Pacific Northwest
NATIONAL LABORATORY

PNNL-30868

Measurements of emanation of Ar-37 and Ar-39 from irradiated rocks and powders

January 2021

Christine Johnson
Justin Lowrey
Thomas Alexander
Emily Mace
Brian Riley

U.S. DEPARTMENT OF ENERGY

Prepared for the U.S. Department of Energy
under Contract DE-AC05-76RL01830

DISCLAIMER

PACIFIC NORTHWEST NATIONAL LABORATORY
operated by
BATTELLE
for the
UNITED STATES DEPARTMENT OF ENERGY
under Contract DE-AC05-76RL01830

Printed in the United States of America

Available to DOE and DOE contractors from the Office of Scientific and Technical Information,
P.O. Box 62, Oak Ridge, TN 37831-0062
www.osti.gov
ph: (865) 576-8401
fax: (865) 576-5728
email: reports@osti.gov

Available to the public from the National Technical Information Service
5301 Shawnee Rd., Alexandria, VA 22312
ph: (800) 553-NTIS (6847)
or (703) 605-6000
email: info@ntis.gov
Online ordering: http://www.ntis.gov

PNNL-30868

Measurements of emanation of Ar-37 and Ar-39 from irradiated rocks and powders

January 2021

Christine Johnson
Justin Lowrey
Thomas Alexander
Emily Mace
Brian Riley

Prepared for
the U.S. Department of Energy
under Contract DE-AC05-76RL01830

Pacific Northwest National Laboratory
Richland, Washington 99354

Abstract

The emanation fraction of radionuclides has been highlighted as a known source of uncertainty in the estimation of radionuclide source signatures from underground nuclear tests and other nuclear activities, particularly in the case of activation products. A system was developed at Pacific Northwest National Laboratory to quantify the emanation fraction of argon from samples ranging in particle size from powder to small rocks. Seven materials, two powders and five rock types, were irradiated with fission spectrum neutrons and the emanation fraction of ^{37}Ar was measured. Additional measurements were made of the ^{39}Ar emanation for four of these materials.

Summary

The radioactive noble gas ^{37}Ar, a potential signature of underground nuclear explosions (UNEs), was one of several gaseous tracers utilized in the larger Pacific Northwest National Laboratory (PNNL) field experiments conducted at the U20az and U12p sites at the Nevada National Security Site (NNSS) under the Underground Nuclear Explosion Signatures Experiment (UNESE). As a result of the impact that gaseous emanation from geologic materials can have on inhibiting the release of argon produced in a UNE, the Argon Release in Soil study filled a major gap in the scientific objectives of UNESE to improve understanding of ^{37}Ar signatures. The study's evaluation of emanation is additionally relevant to the greater UNESE need to understand mechanisms that impact natural gas backgrounds of ^{37}Ar in the shallow subsurface environment.

Early measurements made during the UNESE noble gas migration experiment also highlighted the potential of ^{39}Ar as a long-lived signature of a UNE. Since the same gas processing methods and detector measurement systems are used to quantify ^{39}Ar as those used for ^{37}Ar, additional measurements were made on each sample to quantify the ^{39}Ar emanation.

Two chemical powders, $CaCO_3$ and K_2CO_3, and five rock types (limestone, dolostone, rhyolite, tuff, and obsidian) were irradiated on the Godiva assembly at the NNSS in gas-tight quartz ampoules before being sent to PNNL. Upon return, the samples were opened in a processing manifold and allowed to flow across a cryogenic charcoal trap which captured any argon released from the sample. The argon on this trap was then flowed through a separate gas sampling system and loaded into a proportional counter where the sample was counted for the activity of ^{37}Ar and ^{39}Ar.

For each sample type, the specific production rate of ^{37}Ar and ^{39}Ar was calculated using the ORIGEN code. This expected production rate was then compared to the measured activity of argon in the sample to determine an emanation fraction for both ^{37}Ar and ^{39}Ar.

Acknowledgments

The authors wish to acknowledge the National Nuclear Security Administration, Defense Nuclear Nonproliferation Research and Development, and the Underground Nuclear Explosion Signatures Experiment, a multi-year research and development project sponsored by NNSA DNN R&D and collaboratively executed by Lawrence Livermore National Laboratory, Los Alamos National Laboratory, Mission Support and Test Services, Pacific Northwest National Laboratory, and Sandia National Laboratories. This work was performed by Pacific Northwest National Laboratory under award number DE-AC05-76RL01830.

The Nuclear Criticality Experiments Research Center (NCERC) is supported by the DOE Nuclear Criticality Safety Program, funded and managed by the National Nuclear Security Administration for the Department of Energy.

Acronyms and Abbreviations

HPGe	High-purity germanium
ICP-OES	Inductively coupled plasma optical emission spectrometry
NCERC	Nuclear Criticality Experiments Research Center
NNSS	Nevada National Security Site
PNNL	Pacific Northwest National Laboratory
UNE	Underground nuclear explosion
UNESE	Underground Nuclear Explosion Signatures Experiment
XCT	X-ray computed tomography

Contents

Figures

Tables

1.0 Introduction

The radioactive noble gas ^{37}Ar has been identified as a potential signature of an underground nuclear explosion (UNE) (Haas et al. 2010). Unlike the more traditional UNE signature gases like radioxenon, ^{37}Ar is not a fission product. Instead, ^{37}Ar is generated by activation of the calcium isotope ^{40}Ca (97% natural isotopic abundance) by the reaction ^{40}Ca(n,α)^{37}Ar in the rock surrounding the explosion. This process also occurs naturally in the shallow subsurface through cosmic neutron interactions, resulting in a low background of ^{37}Ar in the subsurface (Riedmann and Purtschert 2011; Johnson et al. 2015).

Recent measurements (McIntyre et al. 2017) have indicated that another radioactive isotope of argon, ^{39}Ar, may also be a potential indicator of a UNE. Natural production of ^{39}Ar in the shallow subsurface is dominated by negative muon capture on ^{39}K (93% natural isotopic abundance) by the reaction $^{-}\mu + {}^{39}K \rightarrow \nu_{\mu} + {}^{39}Ar$ and below approximately 700 meters in rock is dominated by the ^{39}K(n,p)^{39}Ar reaction (Sramek et al. 2017; Mei, Zhang, and Hime 2009). In a UNE, ^{39}Ar will be produced by the ^{39}K(n,p)^{39}Ar reaction in the surrounding media.

Because ^{37}Ar and ^{39}Ar are produced within rocks, atoms must first escape from the rock matrix and into connected pore space before they can be detectable in subsurface gas. In order to make predictions of the potential ^{37}Ar and ^{39}Ar signal from a UNE, a value for this emanation fraction is needed.

1.1 Emanation Fraction

While estimates of ^{37}Ar production rates in various geologies have been made (Johnson et al. 2015; Wilson et al. 2015; Guillon et al. 2016; Fritz et al. 2018), when compared to subsurface measurements (Riedmann and Purtschert 2011; Fritz et al. 2018; Kastlander et al. 2019) the predictions are always significantly higher than the experimental values. This discrepancy can be partially explained by the fact that not all ^{37}Ar (or other activation products such as ^{39}Ar) leave the rock matrix where they are formed to become available for transport and eventual sampling. The emanation fraction, sometimes also referred to as the emanation coefficient, is the fraction of a gas that is able to escape the bulk mineral structure and enter the pore space. The emanation process is highly dependent on a variety of factors which include the grain size and water saturation. Because of its potential health impacts, the emanation fraction of radon is fairly well understood (Sakoda, Ishimori, and Yamaoka 2011), however, the corresponding value for other noble gases is less well studied.

Once argon escapes into the pore space it is partitioned among one of three states: as a gas, available for transport and soil-gas sampling, dissolved in water, or sorbed onto the surrounding media. Measurements of the emanation fraction (termed the fractional release efficiency) from rock to groundwater can be found in Andrews et al. (1991). The system described in this report only considers the gaseous argon which is available for transport.

2.0 Experimental

The following section details each step of the experimental process used to measure the emanation coefficients of ^{37}Ar and ^{39}Ar from calcium-bearing rocks. First, sample rocks were crushed, sieved, and measured for their elemental composition. Second, the sieved rocks (now in powder to pebble-sized pieces) were sealed into quartz ampoules with the air removed and replaced by helium fill gas. The samples were then further encapsulated into aluminum canisters and shipped to the Device Assembly Facility at the Nevada National Security Site (NNSS) where they were neutron irradiated on the Godiva critical assembly. After irradiation, the samples were shipped back to PNNL where the quartz ampoules were broken and the emanated ^{37}Ar and ^{39}Ar gas was cryogenically trapped. This trapped argon was then processed to remove any contaminant gases. Make-up argon that had been extracted from room air was also added to ensure a sufficient total argon gas volume for the proportional counter. This pure argon gas was then loaded into proportional counters for measurement to determine the activity of ^{37}Ar and ^{39}Ar in the samples. The method development and initial results have been previously published in Johnson et al. (2018).

2.1 Sample Materials

Seven sample types were examined in this work: calcium carbonate powder ($CaCO_3$), potassium carbonate powder (K_2CO_3), limestone, dolostone, rhyolitic tuff, obsidian, and rhyolite. The composition of each material was obtained using inductively-coupled plasma optical emission spectrometry (ICP-OES) for the primary elements of interest, but the silicon, oxygen, and carbon content of the sample could not be measured with this method and are assumed to make up the majority of the remaining sample mass. Total carbon was later measured and is shown in Table 1 along with the weight percent of select elements.

Both of the carbonate rock samples (limestone, dolostone) were further broken into different grain sizes. The three grain size ranges examined were >4000 μm, 500-2000 μm, and 250-500 μm. In addition, a single larger piece of limestone weighing approximately 15 grams was examined. For the volcanic rocks, only grains larger than 4000 μm were used.

Table 1. Weight percent [%] of selected elements in each sample type as measured by ICP-OES.

Material	C	Na	Mg	K	Ca	Fe
$CaCO_3$	11.40	0.01	0.002	< 0.02	38.00	0.001
K_2CO_3	8.70	< 0.001	$< 3.08 \times 10^{-5}$	56.60	0.001	$< 1.14 \times 10^{-4}$
Limestone	12.49	< 0.08	0.47	0.25	34.16	0.33
Dolostone	11.11	0.14	7.69	0.93	16.52	0.49
Rhyolite	< 0.02	1.38	0.00	4.52	0.31	0.89
Tuff	< 0.02	2.64	0.01	3.75	0.12	0.62
Obsidian	< 0.02	2.11	0.001	3.89	0.31	0.63

2.2 Sample encapsulation

Prior to irradiation, samples were sealed inside quartz ampoules to contain all the activation products including the gas. The quartz was backfilled with ultra-high purity helium during the sealing process to minimize the impact of the backfill gas on the gas processing system and to minimize gaseous activation products, particularly activated stable argon. The quartz glass chosen for each ampoule was GE214 to reasonably minimize impurities that could contribute to post-irradiation radioactive contaminants. Three ampoule sizes were needed: small ampoules for placement in the center of the assembly and two larger ampoules for placement just outside the assembly. The small ampoules had an outer diameter of 4 mm with a maximum height after heat-sealing of 50 mm. The mid-sized quartz ampoules were approximately 3.8 cm tall with an outer diameter of 3.4 cm and a wall thickness of approximately 1.5 mm, while the largest ampoules had the same diameter and wall thickness but were approximately 11.5 cm tall.

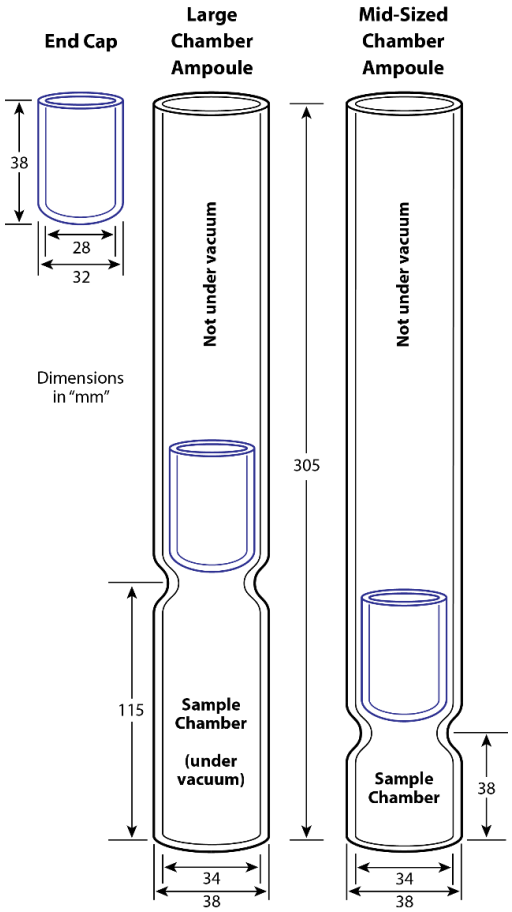

Figure 1. Large (left) and mid-sized (right) ampoules.

Samples were loaded into 30 cm long, 34x38 mm (inner x outer diameter) GE214 fused quartz ampoules with one end sealed while taking care not to leave powders on the inner walls of the ampoule. In the case of the potassium carbonate sample, a secondary cleaning step was needed to remove particles which were attracted to the ampoule walls. The first attempt at creating the potassium carbonate ampoule failed due to a reaction between the potassium carbonate powder and the quartz during fusing. In the second, successful, attempt a cotton swab was used to remove the particles immediately prior to the addition of the end cap.

Next, a fused quartz end cap (3.8 cm long, 28x32 mm; bottom was sealed) was dropped into the vessel and rested on a dimple within the ampoule wall to create the sample chamber. The mid-sized and large ampoules were connected to a vacuum assembly using a 3.8 cm compression fitting where the ampoule was evacuated and flushed with ultra-high purity helium three times. The ampoule was filled to a final pressure of approximately 53.3 kPa and then sealed with an oxy-propane torch. The ampoule designs and dimensions are shown in Figure 1.

Once encapsulated in the quartz ampoules, as seen in Figure 2, the samples were placed in an intermediate aluminum container which served to both protect the samples from the surrounding facility environment and to facilitate ease of shipping the samples. The aluminum canisters were made of 1100 aluminum alloy, which balances machinability with minimization of activation products. The canisters utilize a screw top sealed with a silicone ring to make them gas tight. The container designed for use in the center of the device can fit three ampoules, while the containers placed around the outside of the device can fit one ampoule each.

Figure 2. Dolostone sample in a mid-sized ampoule (left) and, from left to right, rhyolite, tuff, and obsidian samples in large-sized ampoules (right).

The initial aluminum canisters used for the mid-sized ampoules were internally threaded with rubber gasket to ensure the seal. However, when the samples were received post-irradiation, it was discovered that some of the caps had become stuck and could not be removed without destroying the ampoule inside. For the next irradiation a new design was developed which utilized external threads and a cap on both ends of the canister. These were sealed on both ends with PTFE disks. While the design was slightly unwieldy and a bit top-heavy, the changes made it possible to easily remove all the samples post-irradiation. In the instance where a cap had become stuck, the cap on the opposing end was removed instead. Both designs are shown in Figure 3.

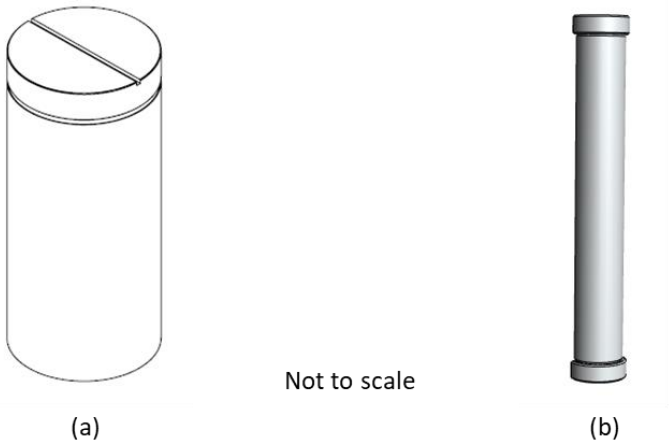

Figure 3. Design of the (a) original mid-sized aluminum canister and (b) the updated large canister.

2.3 Sample irradiation

Three sample irradiations were performed on the Godiva Critical Assembly at the Nuclear Criticality Experiments Research Center (NCERC) located at the NNSS.

The initial irradiation was of two sizes of $CaCO_3$ and was primarily a proof-of concept experiment. Three small ampoules were irradiated in the center of the critical assembly and three medium ampoules were irradiated approximately two inches (centerline) from the assembly's exterior cladding. Because of the decrease in flux at the exterior location, the exterior samples contained significantly more material in order to produce a measurable quantity of ^{37}Ar. The average mass of $CaCO_3$ encapsulated in the small ampoules was 0.08 grams while the average mass of $CaCO_3$ in the large ampoules was 7.0 grams.

In the second irradiation, 13 mid-sized targets were irradiated outside of the assembly with sample masses between 10 and 16 grams. Six of the samples contained dolostone, while the other seven samples contained limestone. Three grain sizes were used for this experiment, with two samples of each size irradiated for each rock type. Additionally, a single 15.5 gram piece of limestone was irradiated as the thirteenth sample.

The third irradiation involved 14 large samples with masses ranging from 48-52 grams and 4 mid-sized samples of masses between 8-9 grams for the powders and approximately 18 grams for the single mid-sized rock sample. These samples were all placed around the exterior of the assembly. Five samples each of obsidian (5 large), rhyolite (5 large), and tuff (4 large, 1 mid) were irradiated in this batch along with two mid-sized samples of $CaCO_3$ powder and one mid-sized sample of K_2CO_3 powder.

The external irradiations were conducted by placing three sample stands around the assembly, with the samples arranged approximately 1.65-cm from the edge of the stand, as shown in Figure 4. A flux foil pack was placed beneath the quartz ampoule, inside of the aluminum canister, in one sample near the center of each stand.

Figure 4. Five mid-sized aluminum canisters, containing a single ampoule each, on the stand used to position the samples around the critical assembly.

2.4 Gas Processing

After irradiation, the encapsulated targets were returned to PNNL for processing and analysis. Before the ^{37}Ar and ^{39}Ar could be measured, the free argon gas had to be removed from encapsulation and trapped for further processing.

After arrival at PNNL, the aluminum canisters were cleaned to remove any external contamination before two of the quartz ampoules were removed from their canisters and screened on a high-purity germanium (HPGe) detector. After the cleaning and screening process, the remaining ampoules were removed from their aluminum canisters and the samples were prepared for gas extraction.

In order to extract the gas from the quartz ampoules, each sample was placed into individual disposable gas volumes which were designed to both break the ampoule and to contain the gas released once the ampoule was broken. Due to thickness of the quartz needed for the ampoules a special crushing device was designed for the large ampoules (see Figure 5 and Figure 6). Filters were installed on both ends of the disposable volumes to prevent any of the sample particles from escaping and contaminating the system.

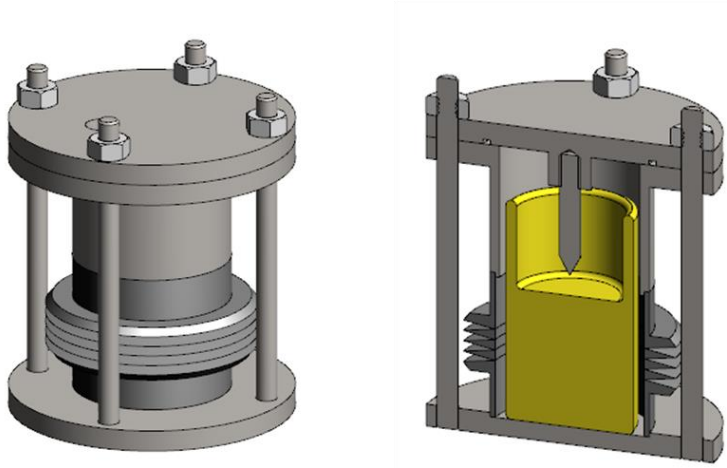

Figure 5. A model of the device used to crush the mid-sized quartz ampoules.

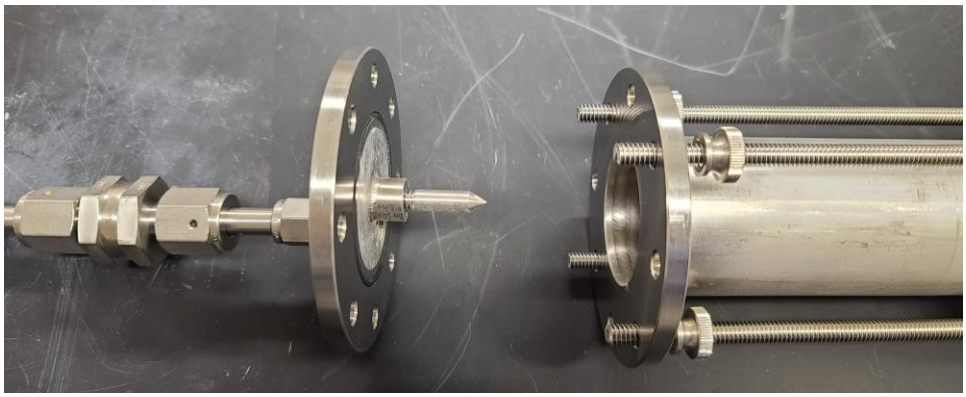

Figure 6. The disposable volume used to crush and contain large quartz ampoules. Visible is the filter used to prevent powder from migrating out of the volume, the O-ring seal, the spike used to puncture the ampoule, and the open volume where the ampoule was placed.

The apparatus used to perform the gas extraction and trapping from the quartz encapsulated samples is a modified version of the system built to measure ^{39}Ar from irradiated powders (Williams et al. 2017). The apparatus is shown in Figure 7 with a mid-sized volume installed. Prior to each sample extraction, the system was vacuumed and flushed with helium to remove as much air and any residual argon from previous samples as possible. The gas processing system and the disposable crushing container were then evacuated to approximately 5.0 torr. Once the system and volume were evacuated and checked for leaks, the system was sealed, and the quartz ampoule was crushed in the disposable volume and the pressure increase recorded. The system was then opened to a cryogenically-cooled charcoal trap designed to trap the argon while allowing the helium to escape via a check valve at the end of the system. In an effort to remove any remaining free argon from the rock and ampoule, ultra-high purity helium was then flowed across the sample and through the charcoal trap for 20 minutes at a pressure of approximately 800 torr. After 20 minutes of helium flow, the charcoal trap was sealed and removed for further processing and loading into a detector system.

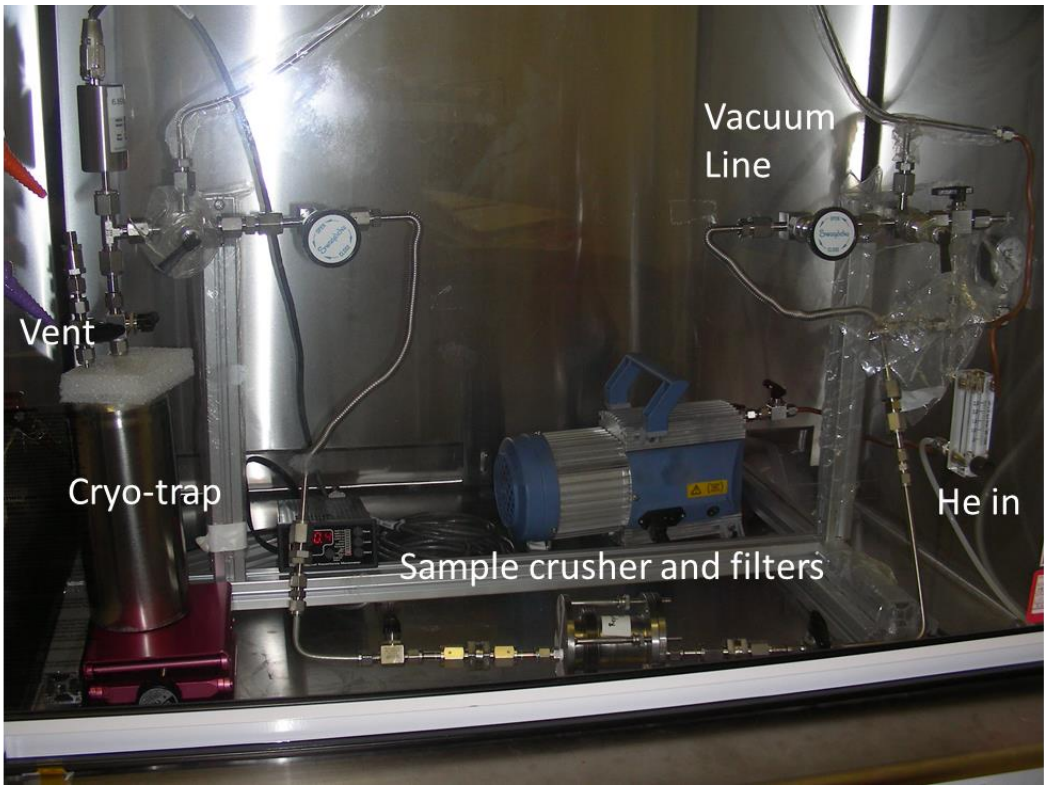

Figure 7. The apparatus used to remove gas from the quartz ampoules and cryogenically trap the argon on charcoal. Shown with a mid-sized sample crusher.

After the extraction and trapping process, the sample was then processed through an additional system designed to separate the argon from any additional gases (including any residual helium). Not enough argon gas was produced in the irradiated samples to provide a complete load for the proportional counters used to detect ^{37}Ar, so room air was flowed through the charcoal trap and into the separation system. The atmospheric argon provided a source of stable argon as make-up gas, but it also forced lingering argon out of the trap at room temperature. The system used for argon separation has been previously described in Alexander et al. (2019). After this processing step, the gas was then loaded into proportional counters to count the activity of ^{37}Ar and ^{39}Ar.

2.4.1 Delayed Emanation Measurements

Repeat measurements were performed on a subset of samples to determine what proportion of the original radioargon remains available for measurement after the initial gas processing removes the accessible argon. After the initial gas processing stage, each sample was sealed in the sample crushing volume and stored.

For the delayed emanation measurements, a stored sample was selected and attached to the gas trapping apparatus. The apparatus was then pumped and flushed using the normal method through the vacuum line so that the sample volume could remain sealed. The remaining process was the same as that used for the standard samples, except that the sample breaker volume was merely opened rather than used to crush the ampoule.

2.5 Detection of ^{37}Ar

After the gas separation and purification, the argon samples were counted in an ultra-low-background gas proportional counter. Inside the proportional counter, the ^{37}Ar is measured via the decays of Auger electron and L-shell x-rays in the gas. The decays of ^{37}Ar form a peak centered at 2.82-keV. The total number of counts in the 2.82-keV peak is found using a Gaussian peak fit with a linear or exponential background term (depending on the background observed at energies above the 2.82-keV peak). The ^{37}Ar activity is found by dividing the total number of counts in the 2.82-keV peak by the ^{37}Ar detection efficiency (Craig E Aalseth et al. 2009; C.E. Aalseth et al. 2011). An example of the ^{37}Ar spectrum used in this analysis is shown for sample E2B in Figure 8.

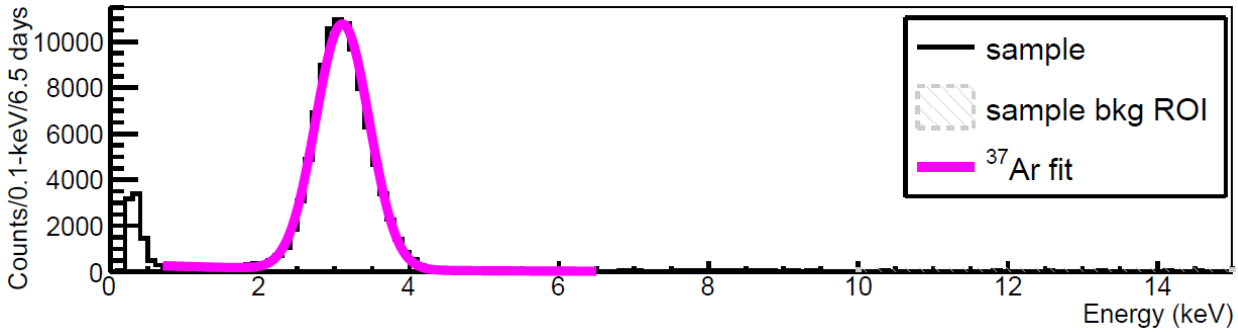

Figure 8. The ^{37}Ar spectrum measured from sample E2B.

2.6 Detection of ^{39}Ar

Like the ^{37}Ar, the ^{39}Ar was also quantified in an internal-source proportional counter. Once ^{37}Ar measurements were complete, the proportional counter gain was recalibrated so that the full ^{39}Ar beta spectrum (0 to 400 keV) was measured. Samples were measured for ^{39}Ar by recalibrating the gain of the proportional counters used in the ^{37}Ar measurement to observe the whole ^{39}Ar beta spectrum, looking from 0 to 400 keV. The analysis was accomplished by subtracting a known background for the detector at the sample pressure and comparing the difference with a spectrum from a known activity “efficiency” from a reference standard gas. An example of the ^{39}Ar spectrum is shown in Figure 9 for one of the irradiated rhyolite samples. The known “efficiency” spectrum in this plot is separate from the efficiency samples discussed later in this work and was used as a known reference to calculate the ^{39}Ar activity against (Williams et al. 2017). Note: the ^{37}Ar peak is still noticeable as a single channel in the first bin of Figure 9.

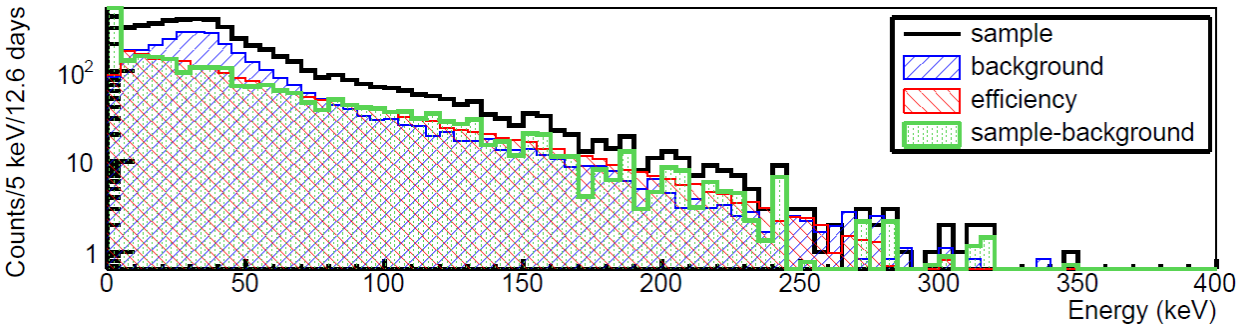

Figure 9. The ^{39}Ar spectrum measured from irradiated rhyolite.

2.7 System efficiency measurement

In order to calculate the percentage of argon that reaches the detector from the sample, a procedure was developed to compare the activity of identical samples before and after the capture and processing steps. Early efforts to measure the system efficiency were unsuccessful due to the use of stable argon as a makeup gas added to samples to aid in the volumetric splitting of the samples. In those efforts the stable argon filled the available space and was able to break through the charcoal trap. This resulted in a significant loss of the radioactive argon and led to the calculation of non-physical results. A new procedure was developed using helium as the makeup gas rather than argon and was used successfully to measure the combined efficiency of the trapping and whole-air separation processes.

Three samples of ^{37}Ar were produced by irradiating three vials approximately 7.5 g of pure $CaCO_3$ powder covered by a helium carrier gas on a 14-MeV D-T neutron generator for approximately 4 hours. A sample of the mixed helium and ^{37}Ar gas produced in the $CaCO_3$ was then pulled from each vial and mixed with additional helium gas. This mixed gas sample was then split into two samples of equal volume, one of which is shown in Figure 10, using a volumetric transfer. After the transfer, each pair of sample coils was left open to each other, but not to atmosphere, for five days to ensure adequate mixing between the samples. A total of six samples, or three sample pairs, were made using this method.

Figure 10. Efficiency sample coil.

The target of these efficiency measurements was to determine the efficiency of the trapping system before the samples were processed. The first of each sample pair, or ‘A’ samples, were expanded into an evacuated SCUBA canister and mixed with dry air that had been aged for over 6 months to minimize the presence of any natural ^{37}Ar. Both containers have known volumes, so the loss of sample to the second volumetric transfer was well quantified. After the sample was expanded and mixed with air, it was then run on the Argon Field System (Hayes et al. 2019) for purification and quantification and the activity of the prepared whole air sample was quantified as a specific activity. The specific activity was then converted to total activity by calculating the absolute activity in the total, well-characterized, volume of the whole-air sample.

The second (‘B’) sample was then placed in-line on the argon trapping system in the same location that the sample crushers were placed. The sample was then processed identically to a standard rock sample. Helium carrier gas was used to flow through the efficiency sample coil and through a cryogenically-cooled charcoal trap. The trapped argon was then removed and separated from the helium carrier using the same system and method as that used for the rock samples. By comparing the activities measured on the ‘A’ and ‘B’ samples, the combined

efficiency of the trapping and whole-air separation steps was calculated. The results of the measurements made on the three sample pairs is shown in Table 2.

Table 2. The ^{37}Ar activity measured in each efficiency sample pair and the resulting system efficiency with uncertainty.

Sample Number	Sample A [Bq]	Sample B [Bq]	System Efficiency	+/-
E1	0.597	0.300	0.503	0.013
E2	0.641	0.336	0.524	0.013
E3	0.551	0.406	0.738	0.024
Average			0.588	0.16

While samples E1 and E2 provided nearly identical efficiency values, sample E3 displayed a notably higher efficiency. An analysis was performed of each step of the efficiency process in an effort to identify any reason for the observed variation, but no anomalies were reported beyond a small increase in the helium carrier flow rate in the E3B sample. It is unlikely that this slight variation in the helium flow would have increased the capture efficiency of the charcoal by upwards of 20%.

3.0 Simulations

In order to calculate the emanation fraction from each sample, the total activation expected in each sample must be calculated. This was done using the COUPLE and ORIGEN modules of SCALE 6.2.2 (Rearden and Jessee 2018). The COUPLE module takes the estimated flux profile of Godiva and calculates single group flux weighted average nuclear cross sections using the specific flux shape. The ORIGEN module then takes those cross sections and combines them with the irradiation flux, time, and the target material composition to determine how much ^{37}Ar is produced per gram of rock.

3.1 Flux-Weighted Cross Sections

In the activation calculations performed by ORIGEN, all energy dependence is embedded in the one-group flux-weighted average cross sections. These calculations are performed by the COUPLE module, which creates a new ORIGEN library specific to the provided energy spectrum. Because GODIVA has a fast neutron spectrum, the JEFF-3.0/A 200-group neutron structure was chosen.

3.2 Production Paths

The reactions identified in ORIGEN as potential paths to produce ^{37}Ar are listed in Table 3 along with their calculated flux-weighted cross section as calculated by COUPLE.

Table 3. The ^{37}Ar producing reactions identified by ORIGEN sorted by their calculated flux-averaged cross sections.

Reaction	Cross Section [b]
^{36}Ar(n,γ)^{37}Ar	7.22×10^{-02}
^{40}Ca(n,α)^{37}Ar	2.27×10^{-02}
^{38}Ar(n,2n)^{37}Ar	1.23×10^{-05}
^{41}Ca(n,n+α)^{37}Ar	6.35×10^{-06}
^{39}K(n,n+d)^{37}Ar	2.48×10^{-08}
^{39}Ar(n,3n)^{37}Ar	9.45×10^{-09}
^{40}K(n,n+t)^{37}Ar	1.59×10^{-11}

While the ^{36}Ar(n,γ)^{37}Ar reaction has the highest cross section, the lack of air present in the samples will minimize this production path. This holds for all reactions where argon is the target element. The only air expected to be in the samples will be that which is trapped within the pore space of the material and was not removed by the vacuum pulled on the sample during encapsulation. The dominant production mechanism will then be the ^{40}Ca(n,α)^{37}Ar reaction.

Like previously shown for ^{37}Ar, the reactions identified in ORIGEN as potential paths to produce ^{39}Ar are listed in Table 4 along with their calculated flux-weighted cross section as calculated by COUPLE.

Table 4. The ^{39}Ar producing reactions identified by ORIGEN sorted by their calculated flux-averaged cross sections.

Reaction	Cross Section [b]
^{39}K(n,p)^{39}Ar	1.48×10^{-01}
^{38}Ar(n,γ)^{39}Ar	1.19×10^{-02}
^{42}Ca(n,α)^{39}Ar	1.66×10^{-03}
^{40}Ar(n,2n)^{39}Ar	1.49×10^{-04}
^{40}K(n,n+p)^{39}Ar	1.32×10^{-04}
^{40}Ca(n,2p)^{39}Ar	3.28×10^{-06}
^{43}Ca(n,n+α)^{39}Ar	6.47×10^{-07}
^{41}Ar(n,3n)^{39}Ar	2.15×10^{-07}
^{41}K(n,n+d)^{39}Ar	1.41×10^{-07}
^{41}Ca(n,^{3}He)^{39}Ar	1.34×10^{-09}
^{42}K(n,n+t)^{39}Ar	8.47×10^{-11}

The (n,p) reaction on ^{39}K has the highest cross section by an order of magnitude and is the dominant production path during neutron irradiation. While neutron capture on ^{38}Ar is also a potentially significant reaction, the low natural abundance of ^{38}Ar (0.06% natural isotopic abundance) and the expected lack of air within the sealed sample ampoules renders this path irrelevant. A similar argument can be made for the (n,α) reaction on ^{42}Ca, since ^{42}Ca has a natural isotopic abundance of only 0.65%.

3.3 Specific Activity Post-Irradiation

Using ORIGEN, the specific activity of ^{37}Ar and ^{39}Ar in Bq/g were calculated for each target material immediately after irradiation. The results of these calculations are shown in Table 5. As expected, the production of ^{39}Ar is significantly reduced in materials with low potassium content, while the ^{37}Ar production decreases significantly in materials with low calcium content. It is worth noting, however, that the production never drops to zero, even in the carbonate powders which contain only one of the elements of interest. In particular, the ^{37}Ar production in the potassium carbonate (K_2CO_3) powder is still in the mBq/g range despite the absence of calcium in this material. From the ICP-OES measurements performed on this powder, calcium is only present in ultra-trace amounts and cannot act as a significant source of ^{37}Ar.

Table 5. The ORIGEN calculated specific activity [Bq/g] of ^{37}Ar and ^{39}Ar immediately post-irradiation.

Target Material	^{37}Ar Bq/g	^{37}Ar Unc [Bq/g]	^{39}Ar Bq/g	^{39}Ar Unc [Bq/g]
Calcium Carbonate	135.67	15.13	3.06×10^{-5}	3.41×10^{-6}
Potassium Carbonate	0.0052	0.0015	0.4616	0.0515
Limestone	121.96	13.60	0.0021	0.0011
Dolostone	58.98	6.58	0.0076	0.0013
Obsidian	1.10	0.12	0.0317	0.0039
Tuff	0.42	0.05	0.0306	0.0037
Rhyolite	1.12	0.13	0.0369	0.0043

In most cases, the uncertainties associated with these values are dominated by the uncertainty in the neutron fluence (11.15%). However, in a few cases the uncertainty in the potassium

content of the rock dominates, particularly in the case of limestone (51%). The uncertainty quantification also assumes that the nuclear cross-section values are accurate to within 10% at the relevant energies.

3.4 Calculating predicted activities

Production of ^{37}Ar and ^{39}Ar is through activation reactions. Calculations of the expected activity of ^{37}Ar and ^{39}Ar were performed using the ORIGEN solver of SCALE 6.2.2. ORIGEN solves the system of ordinary differential equations that describe nuclide generation, depletion, and decay.

$$\frac{dN_i}{dt} = \sum_{j \neq 1} \left(l_{ij}\lambda_j + f_{ij}\sigma_j \Phi\right) N_j(t) - (\lambda_i + \sigma_i \Phi) N_i(t) \quad (1)$$

N_i= amount of nuclide i (atoms)

λ_i = decay constant of nuclide i (1/s)

l_{ij} = fractional yield of nuclide i from decay of nuclide j

σ_i = spectrum-averaged removal cross section for nuclide i (barns)

f_{ij} = fractional yield of nuclide i from neutron-induced removal of nuclide j

Φ = angle- and energy-integrated time-dependent neutron flux (neutrons/cm^2-s)

Here, the spatial dependence is encompassed in Φ, or the spatially-averaged neutron flux magnitude. Energy dependence is encompassed in σ_j, or the one-group flux-weighted average cross sections (described above) and in f_{ij}, the flux-weighted average reaction yields.

For each sample material, the composition (from ICP-OES) was input as fractions of a gram, so that the total mass input is one gram. This simplifies calculations across a range of sample masses but neglects the potential for self-shielding in larger samples. Only the dominant elements are included, typically calcium, potassium, iron, and sodium.

GODIVA irradiations are burst irradiations, so the total irradiation time is assumed to be one millisecond. This is multiplied with the neutron flux (neutrons/cm^2-s) to determine the neutron fluence (neutrons/cm^2), the value used to calculate the total number of interactions.

Using the specific activities from Table 5 and the known mass of each sample, the total predicted ^{37}Ar activity immediately post-irradiation, $A_{0_{Ar-37}}$, and ^{39}Ar activity, $A_{0_{Ar-39}}$, can be calculated for each sample. These values are then decay-corrected from the date of irradiation to the measurement date.

$$A_{Ar-37_{predicted}} = A_{0_{Ar-37}} e^{-\lambda_{Ar-37}(t_c - t_i)} \quad (2)$$

The same decay correction was performed for the ^{39}Ar values, but because of the long half-life of ^{39}Ar, the impact on the final values was negligible.

Losses during the gas processing between the charcoal trap and the detector are captured in two efficiency values, ϵ_{PQ} and ϵ_{QD}. The value for ϵ_{PQ} is constant for the system and has been measured as 0.675. The efficiency ϵ_{QD} is run-specific and is calculated during the gas processing step. With these values, the activity of ^{37}Ar predicted to be in the detector can be calculated as:

$$A_{Ar-37_{predicted_d}} = \epsilon_{PQ}\epsilon_{QD}A_{0_{Ar-37}}e^{-\lambda_{Ar-37}(t_c-t_i)} \quad (3)$$

This value is the predicted ^{37}Ar activity in the detector if all the ^{37}Ar produced during irradiation was available for gas transport.

3.5 Calculating emanation fraction

Once the ^{37}Ar or ^{39}Ar samples are counted, the emanation fraction, ε, can be calculated by taking the ratio of the measured activity to the predicted total activity from Equation (3).

$$\varepsilon = \frac{A_{Ar-37\ measured}}{A_{Ar-37_{predicted_d}}} \quad (4)$$

3.6 Uncertainty Quantification

The emanation fraction calculated in Equation (4) is a combination of multiple values, each with associated uncertainties.

The calculated specific activity of argon post-irradiation for each sample material, S is listed in Table 5. In its simplest form, the equation used to calculate S is:

$$S = \frac{cN_A}{M}\sigma_{Ar}\phi(1 - e^{-\lambda t}) \quad (5)$$

Where c is the concentration of calcium or potassium in the sample, N_A is Avogadro's number, M is the molar mass of the target, σ_{Ar} is the argon production cross section, and ϕ is the neutron flux from the reactor.

The associated uncertainties, σ_S, can then be calculated

$$\sigma_S = S\sqrt{\left(\frac{\sigma_\phi}{\phi}\right)^2 + \left(\frac{\sigma_c}{c}\right)^2} \quad (6)$$

The predicted argon activity in each sample is then calculated to be the specific production rate S times the measured sample mass m_{meas} which leads to an uncertainty in $A_{Ar_{predicted}}$ of $\sigma_{A_{Ar_{predicted}}}$.

$$\sigma_{A_{Ar_{predicted}}} = A_{Ar_{predicted}}\sqrt{\left(\frac{\sigma_S}{S}\right)^2 + \left(\frac{\sigma_{m_{meas}}}{m_{meas}}\right)^2} \quad (7)$$

Because the uncertainty in the measured mass of each sample m_{meas} is low (0.001 g), $\sigma_{A_{Ar_{predicted}}}$ will be dominated by σ_S.

For Equation (3), the uncertainty arises in the two efficiency values ϵ_{PQ} and ϵ_{QD}. These two values can be combined into a single efficiency value, ϵ_S with a known uncertainty of σ_{ϵ_S}. This value then contributes to the uncertainty in the production activity expected in the detector $A_{Ar_{predicted}}{}_d$.

$$\sigma_{A_{Ar_{predicted}}{}_d} = A_{Ar_{predicted}}{}_d \sqrt{\left(\frac{\sigma_{A_{Ar_{predicted}}}}{A_{Ar_{predicted}}}\right)^2 + \left(\frac{\sigma_{\epsilon_S}}{\epsilon_S}\right)^2} \tag{8}$$

This value, along with the reported uncertainty in the measured argon activity $\sigma_{A_{meas}}$, then contributes directly to the uncertainty in the measured emanation values σ_ε.

$$\sigma_\varepsilon = \varepsilon \sqrt{\left(\frac{\sigma_{A_{Ar_{predicted}}{}_d}}{A_{Ar_{predicted}}{}_d}\right)^2 + \left(\frac{\sigma_{A_{meas}}}{A_{meas}}\right)^2} \tag{9}$$

4.0 XCT Imaging of Solid Samples

A representative piece of each solid rock type was imaged using x-ray computed tomography (XCT). Within each image, pore space within the rock was highlighted and used to compute a porosity, permeability, and tortuosity for each sample as shown in Table 6. No permeability or porosity were measured for obsidian since no connected pore space was detected.

Table 6. Flow parameters measured by XCT for each rock sample type.

Material	Porosity [%]	Permeability [Darcy]	Tortuosity	Voxel Size [mm]
Dolostone	9.08	195.9	1.64	0.0167
Limestone	5.60	0.0037	1.57	0.0129
Tuff	0.70	0.0047	1.60	0.0172
Obsidian	0.04	NM	NM	0.0158
Rhyolite	1.11	0.0468	1.39	0.0202

4.1 Dolostone

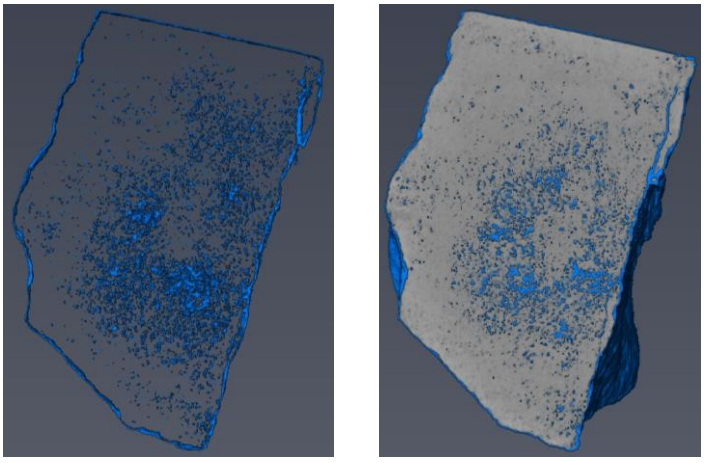

Figure 11. An XCT image of dolostone showing (left) the pores identified in the sample and (right) the CT scanned image with the pores highlighted.

4.2 Limestone

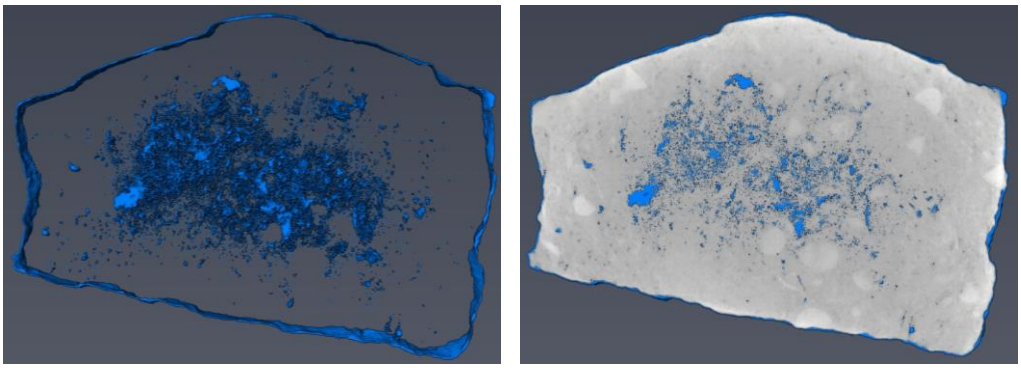

Figure 12. An XCT image of limestone showing (left) the pores identified in the sample and (right) the CT scanned image with the pores highlighted.

4.3 Tuff

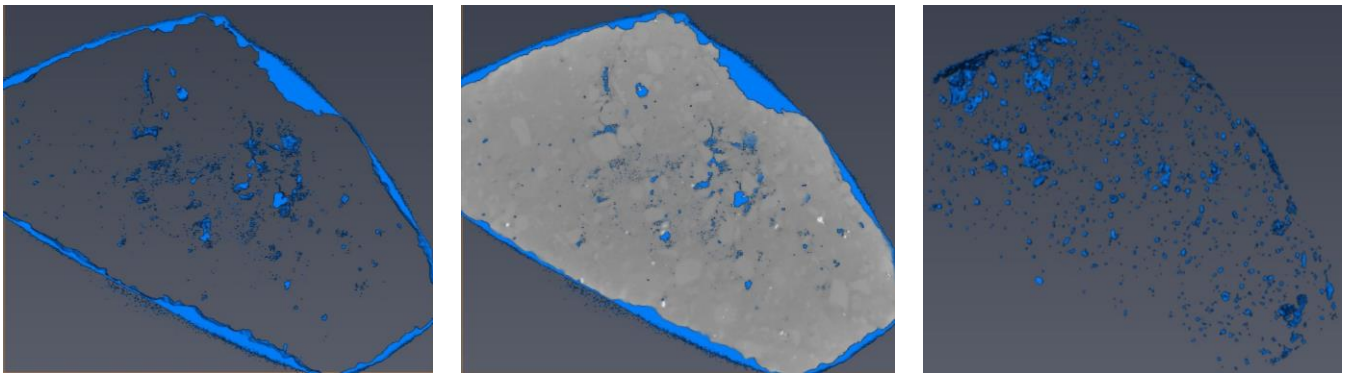

Figure 13. An XCT image of tuff showing (left) the pores identified in the sample, (center) the CT scanned image with the pores highlighted, and (right) high-density particles present in the sample.

4.4 Obsidian

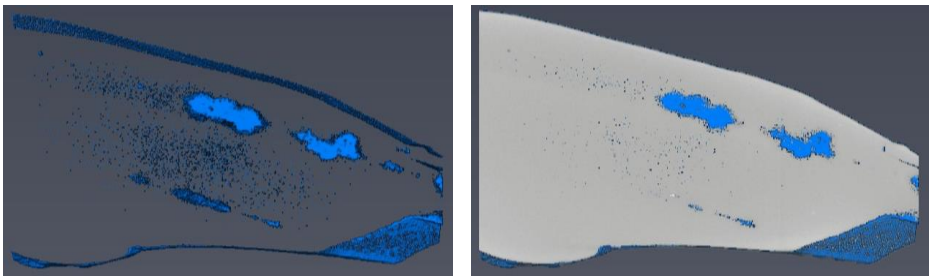

Figure 14. An XCT image of obsidian showing (left) the pores identified in the sample and (right) the CT scanned image with the pores highlighted.

4.5 Rhyolite

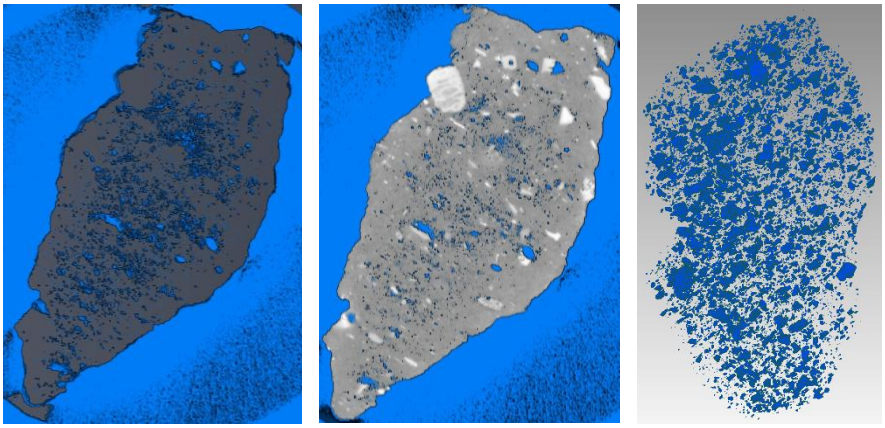

Figure 15. An XCT image of rhyolite showing (left) the pores identified in the sample, (center) the CT scanned image with the pores highlighted, and (right) high-density particles present in the sample.

5.0 Results

5.1 Emanation measurements

Each sample was processed and counted using the method described in the previous sections. The ^{37}Ar measured in each sample, decay-corrected to the irradiation date, is shown in Table 7 along with the percent emanation calculated using Equation 4.

Table 7. Sample mass and measured ^{37}Ar activity decay corrected to the irradiation date. The estimated fractional release (emanation) is also reported.

Material	Mass [g]	Grain Size [μm]	^{37}Ar Activity [Bq]	^{37}Ar Unc. [Bq]	Emanation [%]	Emanation Unc. [%]
Ca Carbonate	8.58	<<250	6.00	0.021	1.49	0.44
K Carbonate	9.000	<<250	0.0049	0.0005	25.1	10.31
Dolostone	10.164	250-500	1.572	0.038	0.68	0.68
Dolostone	12.640	500-2000	1.108	0.034	0.41	0.41
Dolostone	12.269	>4000	0.839	0.045	0.42	0.42
Limestone	10.983	250-500	7.167	0.012	1.93	0.57
Limestone	12.479	500-2000	12.26	0.113	2.12	0.62
Limestone	12.066	>4000	5.833	0.085	1.95	0.57
Consolidated Limestone	15.477	>>4000	9.863	0.17	1.40	0.41
Tuff	50.17	>4000	1.308	0.012	19.13	5.67
Tuff	50.46	>4000	1.136	0.014	14.11	4.19
Obsidian	50.45	>4000	0.027	0.003	0.11	0.03
Obsidian	50.60	>4000	0.019	0.001	0.10	0.03
Rhyolite	50.49	>4000	0.680	0.010	3.73	1.10
Rhyolite	50.03	>4000	1.389	0.023	5.99	1.78
Rhyolite	49.92	>4000	0.814*	0.207	4.35	1.70

Emanation fractions were calculated by comparing the activity produced via activation, calculated using the ORIGEN module in SCALE 6.2.2, and the activity released from the irradiated material, calculated as the measured activity divided by the system efficiency.

The ^{39}Ar measured in each sample is shown in Table 8. Because ^{39}Ar is produced much more readily in samples containing appreciable concentrations of potassium, it was expected that ^{39}Ar levels would be much lower in the dolostone and limestone with their much lower K concentrations. This trend was observed, with no detectable ^{39}Ar observed in the limestone sample and with low ^{39}Ar activities observed on the dolostone sample. The $CaCO_3$ samples (no K) were not measured for ^{39}Ar.

Table 8. Sample mass and measured ^{39}Ar activity decay corrected to the irradiation. The estimated fractional release (emanation) is also reported. The activities reported here are activities above atmospheric levels.

Material	Mass	Grain Size [μm]	^{39}Ar Activity [Bq]	^{39}Ar Uncertainty [Bq]	Emanation [%]	Emanation Unc. [%]
K Carbonate	9.000	<<250	0.187	0.002	10.97	3.23
Tuff	50.17	>4000	0.003	0.0003	0.54	0.17
Tuff	50.46	>4000	0.002	0.00008	0.36	0.11
Obsidian	50.45	>4000	0.0003	0.00005	0.04	0.01
Obsidian	50.60	>4000	<1E-06	ND	ND	0.0002
Rhyolite	50.49	>4000	0.002	0.00008	0.37	0.11
Rhyolite	50.03	>4000	0.004	0.0002	0.47	0.14
Dolostone	12.54	>4000	0.0004	5.88E-05	1.50	0.53
Limestone	10.75	250-500	<7.8E-05	ND	ND	0.69

5.2 Delayed emanation measurements

The results of the delayed emanation measurements for ^{37}Ar are shown in Table 9 and for ^{39}Ar in Table 10. The days between processing column lists the number of days that passed between the initial processing of the sample and the processing of the repeat sample.

Table 9. Measured ^{37}Ar activity in repeat measurements. The * denotes a sample for which the ampoule did not fully break.

Material	Mass	Grain Size [μm]	^{37}Ar Activity [Bq]	^{37}Ar Uncertainty [Bq]	Emanation [%]	Emanation Unc. [%]	Days Between Processing
Ca Carbonate	9.000	<<250	0.073	0.011	0.01	0.003	261
Tuff	50.17	>4000	0.064	0.010	0.57	0.19	230
Tuff	50.46	>4000	0.876	0.078	8.30*	2.57	203
Rhyolite	50.49	>4000	0.239	0.058	0.75	0.29	199
Rhyolite	49.92	>4000	ND	ND	ND	ND	0.06

Table 10. Measured ^{39}Ar activity in repeat measurements. The * denotes a sample for which the ampoule did not fully break.

Material	Mass	Grain Size [μm]	^{39}Ar Activity [Bq]	^{39}Ar Uncertainty [Bq]	Emanation [%]	Emanation Unc. [%]	Days Between Processing
Tuff	50.17	>4000	6.461E-05	4.740E-05	0.01	0.01	230
Tuff	50.46	>4000	1.414E-03	6.041E-05	0.26*	0.08	203
Rhyolite	50.49	>4000	7.297E-04	5.427E-05	0.11	0.03	199

6.0 Discussion

The emanation fraction represents a potentially significant source of uncertainty in models of activation product yield estimates from UNEs and in predicting natural gas backgrounds. This work, first and foremost, details and demonstrates the method developed by PNNL to measure the ^{37}Ar and ^{39}Ar released from rocks and powders that have been irradiated. Due to the inherent variability of geologic materials, rocks of similar type from location to location, or even different parts of the same formation, are likely to result in different emanation fractions. As a result, the emanation values reported here are of some limited value specific to the rocks examined under the conditions they were irradiated and analyzed. It is, therefore, important to examine these results for correlations that might help extend their relevance to more general locations.

6.1 Emanation of ^{37}Ar versus ^{39}Ar

Comparing results of Table 7 and Table 8, in all cases the percent emanation of ^{37}Ar was significantly higher than that of ^{39}Ar. This may be due in part to the difference in the energetics of the argon producing reactions. For the ^{40}Ca(n,α)^{37}Ar reaction the recoil range of the ^{37}Ar atom is 408.4 nm (Onstott et al., 1995). By comparison, the mean recoil range of the ^{39}Ar atom produced by the ^{40}K(n,p)^{39}Ar reaction is only 175.6 nm (Onstott et al., 1995).

If an argon atom is not emitted into the pore space through recoil it may still be transported through diffusion. Since ^{37}Ar and ^{39}Ar are both radioactive, the diffusion path length is limited by the lifetime of the atom and is related to the effective diffusion coefficient of argon in the matrix, D_{eff}, as $L = (D_{eff} / \lambda)^{1/2}$. In the case of a crystal lattice, the D_{eff} of argon is $<10^{-26}$ m^2 s^{-1}, so the diffusion path length over the lifetime of ^{37}Ar is <0.2 nm while the longer-lived ^{39}Ar has a diffusion path length of <11 nm (R. a Riedmann and Purtschert, 2011; Watson and Cherniak, 2003).

The shorter half-life of ^{37}Ar would seem to preclude that emanation is purely dominated by matrix diffusion effects, as has been argued previously in Andrews et al. (1991) who concluded that release of ^{37}Ar and ^{39}Ar must be surface dominated. Hess (1986) also observed higher emanation fractions for ^{37}Ar versus ^{39}Ar. If the measured activities of ^{37}Ar and ^{39}Ar are converted into number of atoms, the ratios of ^{37}Ar/^{39}Ar measured in this work and shown in Table 11 are similar (but slightly higher) to those reported by (Hess 1986), with the exception of the potassium carbonate sample.

Table 11. The measured ratios of ^{37}Ar/^{39}Ar atoms in each material. For materials with multiple measurements, the average result is reported.

	Atoms of ^{37}Ar/^{39}Ar
Rhyolite	0.116
Tuff	0.185
Obsidian	0.032
Potassium Carbonate	9.22×10^{-6}
Dolostone	0.696

6.2 Temperature and impact of emanation on natural production

The emanation rates reported in this work are likely indicative of conditions near room temperature. However, it must be noted that when irradiated, the samples would have experienced temperature fluctuations due to neutron heating. As a result, temperature was not a strictly controlled variable in this study. While the results of this work cannot completely deconvolve the relative impact of atomic recoil energy versus gas transport effects in determining emanation fractions, it can be assumed that factors like sorption can influence how much argon moves freely in the pore space of rocks. Since surface adsorption is temperature dependent, it is expected that argon emanation is likely to increase as a function of temperature. Because the values provided here were nominally obtained at room temperature, they are almost certainly conservative estimates of the levels of ^{37}Ar and ^{39}Ar that might be expected to be emitted in a UNE, where extreme temperatures (not to mention rock crushing and vaporization) would have additional impact not addressed here. However, the emanation fraction values reported here are likely be more directly relevant for predictions of the natural background level of radioargon.

In recent literature, assumptions have been made that the ^{37}Ar emanation rate ranges between 2-7% (Fritz et al., 2018; Guillon et al., 2016; R. a Riedmann and Purtschert, 2011). In most cases, the results reported here fall into that range or slightly below. For the rock samples considered in this work, only one material (the tuff) exceeded this range. However, most samples, particularly the carbonates, fell at or below the low end of the 2-7% range. This means that predictions, like those made by Fritz et al. (2018), using the higher values may overestimate the amount of argon available for transport. In examining the results of Fritz et al. (2018), this may be the case in the high calcium samples, where the predictive model consistently overestimated the expected ^{37}Ar in the subsurface.

6.3 Variability in ampule failure

At the end of the sample measurement campaign, the ampoule crushing volumes were unloaded and the final disposition of the quartz ampoules was noted. In almost all cases major failures in the quartz ampoule was observed. In general, the medium ampoules were more thoroughly broken than the large ampoules. In Figure 16 three examples of broken ampoules are shown. While the majority of the medium ampoules were thoroughly destroyed like shown in Figure 16a, the large ampoules had a greater variety in the degree of destruction from complete ampoule failure as shown in Figure 16b and destruction of only the bottom of the ampoule as shown in Figure 16c. The emanation calculation assumes 100 percent removal of available argon from each sample, so incomplete ampoule destruction may contribute some additional uncertainty.

Figure 16. Broken ampoules for (a) Sample 17 (limestone), (b) Sample 32 (rhyolite), and (c) Sample 41 (tuff).

In one case, that of sample 45, the quartz ampoule was not broken. Instead, a single hole was punched through the bottom of the ampoule by the spike (Figure 17). This likely explains the unexpectedly high activity remaining in sample 45 during the delayed emanation measurement. With the hole likely blocked by the puncturing spike, the helium flow was not able to properly circulate and remove all of the radioargon from the gas surrounding the irradiated tuff.

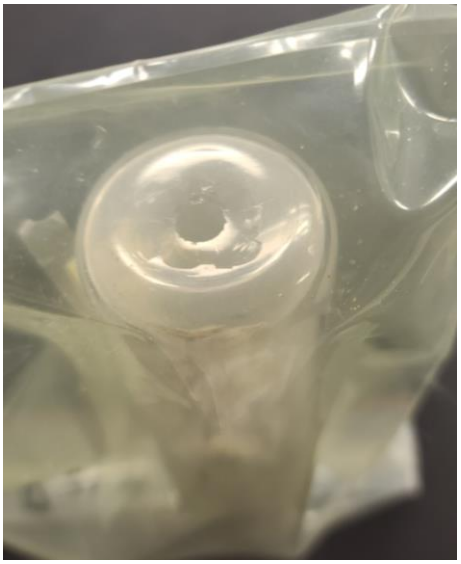

Figure 17. The punctured quartz ampoule of sample 45.

6.4 Conceptual model of repeat measurements

Given the assumption that emanation might be partially a function of how gas moves within the bulk rock matrix after it is produced, it was predicted that some fraction of produced argon gas initially bound within the rock could diffuse (or otherwise transport) into the connected pore space over time. Repeat measurements of the argon emanation were made of a subset of

samples and some preliminary assessment of these measurements can be made with a “toy model” type of approach, which is outlined here.

The sample volume can be broken into three regions – the volume of space occupied by the rock sample, V_{rock}, the volume of the rock that is connected pore space, V_{pore}, and the volume of the ampoule that is free gas space V_{gas}. Assuming:

$$V_{gas} = \frac{1}{2} V_{amp}$$

$$V_{rock} = \frac{1}{2} V_{amp}$$

$$V_{pore} = \frac{1}{3} V_{rock}$$

where the last equation is assuming a 33% porosity. Then

$$V_{pore} = \frac{1}{6} V_{amp}$$

If it is assumed that only the radioargon in the gas volume is sampled during processing of the sample, and that prior to measurement the argon concentration has had enough time to equilibrate throughout, then the fraction of emanated argon that is measured during the first round of sample processing can be calculated.

$$V_{gas} = 3V_{pore}$$

$$A_{gas}(0) = 3A_{pore}(0)$$

If it is assumed that all of the emanated argon is present in either the gas volume or the connected pore volume, then the amount of argon present in the connected pore space can be equated to the total emanated argon at time 0 by

$$A_{gas}(0) = 3A_{pore}(0)$$

$$A_E = A_{gas} + A_{pore} = 3A_{pore}(0) + A_{pore} = 4A_{pore}$$

And if it is assumed that all free argon from the gas volume is removed and measured during the initial measurement period then the percentage of measured argon that is measured can be equated to what remains in the vial by

$$A^1_{remain} = \frac{1}{4} A_E$$

$$A^1_{meas} = 0.75 A_E$$

For the second measurement of emanated argon, the delayed emanation measurement, the calculation must also take into account the additional gas volume provided by the crushing volume that contains the sample once the ampoule was broken. If it is assumed that the ampoule volume was roughly 80% of the crusher volume, the volumes can then be defined as

$$V_{crush} = 1.25V_{amp}$$

$$V_{crush} = 1.25\left(6V_{pore}\right) = 7.5V_{pore}$$

And if it is assumed that the argon has evenly distributed between the crusher gas volume and the connected pore space then the remaining activity can be defined as

$$A^1_{remain} = A_{crush} + A_{pore} = 8.5A_{pore}$$

Assuming that only the gas present in the crusher volume is measured, then the second measurement should be defined as

$$A^2_{remain} = \frac{1}{8.5}A^1_{remain} = 0.12(0.25)A_E = 0.029A_E$$

$$A^2_{meas} = \frac{8.5-1}{8.5}A^1_{remain} = 0.88(0.25)A_E = 0.22A_E$$

More generally, the ratio of a repeated measurement with the original estimate can be written for porosity, ϕ, as

$$\frac{A^2_{meas}}{A^1_{meas}} = \frac{2.5\phi}{2.5+\phi}$$

Applying this equation to data in the preceding tables for those samples that had repeated measurements is summarized in Table 12. The ratios of repeated measurements is consistently under-predicted by more than an order of magnitude. There are at least two very likely reasons for this. Firstly, porosities used in the above ratio calculation are based on XCT measurements of samples and likely significantly under predicted. Secondly, the toy model makes some significant assumptions and simplifications in how true emanation likely occurs. For instance, it assumed that the A^1_{meas} is 100% efficient in capturing all free argon gas in the ampoule; if this isn't the case, which is likely, then the A^1_{remain} model estimate will be accordingly undervalued and lead to a lower A^2_{meas} estimate. This is only one likely culprit, but it is worth pointing out that using more reasonable values for sample porosity (1-10% range) results in much closer agreement between measured and modeled ratios.

Table 12. Ratios of repeated measurements made examining emanation over time compared with toy model estimates based on porosity.

Material	Mass	$^{37}Ar_1$ Activity [Bq]	$^{37}Ar_1$ Emanation [%]	$^{37}Ar_2$ Activity [Bq]	$^{37}Ar_2$ Emanation [%]	$^{37}Ar_2/^{37}Ar_1$ (measured)	$^{37}Ar_2/^{37}Ar_1$ (ϕ predicted)
Tuff	50.17	1.308	19.13	0.064	0.57	0.0298	0.0100
Tuff	50.46	1.136	14.11	0.876	8.30*	0.588	0.0070
Rhyolite	50.49	0.680	3.73	0.239	0.75	0.201	0.0111
Material	Mass	$^{39}Ar_1$ Activity [Bq]	$^{39}Ar_1$ Emanation [%]	$^{39}Ar_2$ Activity [Bq]	$^{39}Ar_2$ Emanation [%]	$^{39}Ar_2/^{39}Ar_1$ (measured)	$^{39}Ar_2/^{39}Ar_1$ (ϕ predicted)
Tuff	50.17	0.003	0.54	6.461E-05	0.01	0.0185	0.0070
Tuff	50.46	0.002	0.36	1.414E-03	0.26*	0.722	0.0070
Rhyolite	50.49	0.002	0.37	7.297E-04	0.11	0.297	0.0111

7.0 Conclusions

Prior to this work, estimations of activation product production rates, whether in relation to UNE events or from natural background production in the subsurface, have largely ignored the emanation process entirely. In other instances, emanation has been relied upon as a mysterious "fudge-factor" relied upon to vaguely account for discrepancies between predicted levels and experimentally measured values of activation product gases. The primary goal of this work was to develop a method for directly measuring argon emanation fractions and to demonstrate that method with a handful of initial measurements.

This report summarizes all the measurements made of ^{37}Ar and ^{39}Ar emanation. In all instances where both isotopes were measured from the same sample, the emanation fraction of ^{37}Ar was estimated to be larger than that of ^{39}Ar. Since ^{39}Ar has a significantly longer half-life than ^{37}Ar, it is concluded that the smaller ^{39}Ar emanation is likely due to a difference in recoil energy in the activation reactions.

Significant variability was observed among the emanation rates across various geologic materials. The rate of ^{37}Ar emanation from irradiated geologic materials was found to be highly variable across different rock types. For limestone and dolostone, little variation in ^{37}Ar emanation was observed when the size of irradiated materials was varied from 250 ->4000 μm. With the exception of obsidian, the ^{37}Ar emanation rate was significantly higher for the volcanic rocks than the carbonates. The obsidian emanation rate was the lowest of all of the irradiated materials, likely due to its glassy nature and lack of connected pore space. The emanation rate of ^{39}Ar was measured for three volcanic rocks and potassium carbonate and was observed to be significantly (55-95%) lower in all cases than that of ^{37}Ar.

8.0 References

Aalseth, C.E., a.R. Day, D.a. Haas, E.W. Hoppe, B.J. Hyronimus, M.E. Keillor, E.K. Mace, J.L. Orrell, a. Seifert, and V.T. Woods. 2011. “Measurement of 37Ar to Support Technology for On-Site Inspection under the Comprehensive Nuclear-Test-BanTreaty.” *Nuclear Instruments and Methods in Physics Research Section A: Accelerators, Spectrometers, Detectors and Associated Equipment* 652 (1): 58–61. https://doi.org/10.1016/j.nima.2010.09.135.

Aalseth, Craig E, Anthony R Day, Eric W Hoppe, Todd W Hossbach, Brian J Hyronimus, Martin E Keillor, Kevin E Litke, Esther E Mintzer, Allen Seifert, and Glen A Warren. 2009. “Design and Construction of a Low-Background , Internal-Source Proportional Counter.” *Journal of Radioanalytical and Nuclear Chemistry* 282: 233–37. https://doi.org/10.1007/s10967-009-0258-5.

Alexander, T. R., C. E. Aalseth, H. O. Back, T. W. Bowyer, A. R. Day, E. S. Fuller, J. C. Hayes, et al. 2019. “Characterization of a Low Background Proportional Counter for a High Throughput Argon-37 Collection and Measurement System.” *Nuclear Instruments and Methods in Physics Research, Section A: Accelerators, Spectrometers, Detectors and Associated Equipment*, no. July 2018: 1–6. https://doi.org/10.1016/j.nima.2019.01.021.

Andrews, J. N., T. Florkowski, B. E. Lehmann, and H. H. Loosli. 1991. “Underground Production of Radionuclides in the Milk River Aquifer, Alberta, Canada.” *Applied Geochemistry* 6 (4): 425–34. https://doi.org/10.1016/0883-2927(91)90042-N.

Fritz, Bradley G., Craig E. Aalseth, Henning O. Back, James C. Hayes, Paul H. Humble, Pavlo Ivanusa, and Emily K. Mace. 2018. “Prediction of Sub-Surface 37 Ar Concentrations at Locations in the Northwestern United States.” *Journal of Environmental Radioactivity* 181 (October 2017): 1–7. https://doi.org/10.1016/j.jenvrad.2017.10.005.

Guillon, Sophie, Yunwei Sun, Roland Purtschert, Lauren Raghoo, Eric Pili, and Charles R. Carrigan. 2016. “Alteration of Natural 37Ar Activity Concentration in the Subsurface by Gas Transport and Water Infiltration.” *Journal of Environmental Radioactivity* 155–156: 89–96. https://doi.org/10.1016/j.jenvrad.2016.02.021.

Haas, DA, JL Orrell, TW Bowyer, and JI McIntyre. 2010. “The Science Case for 37Ar as a Monitor for Underground Nuclear Explosions.” PNNL-19458. http://www.pnl.gov/main/publications/external/technical_reports/PNNL-19458.pdf.

Hayes, J, C Aalseth, T Alexander, H Back, E Church, M Foxe, T Hossbach, et al. 2019. “High Throughput Argon-37 Field System.” *Manuscript Submitted for Publication*.

Hess, J. 1986. “Kinetics of Ar Isotopes during Neutron Irradiation: 39Ar Loss from Minerals as a Source of Error in 40Ar/39Ar Dating.” *Chemical Geology* 59 (4): 223–36. https://doi.org/10.1016/0009-2541(86)90047-1.

Johnson, Christine, Hirotatsu Armstrong, William H Wilson, and Steven R Biegalski. 2015. “Examination of Radioargon Production by Cosmic Neutron Interactions.” *Journal of Environmental Radioactivity* 140 (November): 123–29. https://doi.org/10.1016/j.jenvrad.2014.10.016.

Johnson, Christine, Amanda Prinke, Justin D. Lowrey, Paul Humble, Emily Mace, Thomas Alexander, Brian J. Riley, and Richard Williams. 2018. “A Method to Quantify the 37Ar Emanation Fraction in Powders and Rocks.” *Journal of Radioanalytical and Nuclear Chemistry* 318 (1): 297–303. https://doi.org/10.1007/s10967-018-6024-9.

Kastlander, J., M. Aldener, T. Fritioff, L. Raghoo, and R. Purtschert. 2019. “Measurement of Radioxenon and Radioargon in Air from Soil with Elevated Uranium Concentration.” *Journal of Environmental Radioactivity* 197 (July 2018): 62–66. https://doi.org/10.1016/j.jenvrad.2018.12.006.

McIntyre, J.I., C.E. Aalseth, T.R. Alexander, H.O. Back, B.J. Bellgraph, T.W. Bowyer, V. Chipman, et al. 2017. “Measurements of Argon-39 at the U20az Underground Nuclear Explosion Site.” *Journal of Environmental Radioactivity* 178–179: 28–35. https://doi.org/10.1016/j.jenvrad.2017.07.013.

Mei, D. M., C. Zhang, and A. Hime. 2009. “Evaluation of (a, n) Induced Neutrons as a Background for Dark Matter Experiments.” *Nuclear Instruments and Methods in Physics Research, Section A: Accelerators, Spectrometers, Detectors and Associated Equipment* 606 (3): 651–60. https://doi.org/10.1016/j.nima.2009.04.032.

Rearden, B T, and M A Jessee. 2018. “SCALE Code System.” *ORNL/TM-2005/39*.

Riedmann, Robin A, and Roland Purtschert. 2011. “Natural 37Ar Concentrations in Soil Air: Implications for Monitoring Underground Nuclear Explosions.” *Environmental Science & Technology* 45 (20): 8656–64. https://doi.org/10.1021/es201192u.

Sakoda, Akihiro, Yuu Ishimori, and Kiyonori Yamaoka. 2011. “A Comprehensive Review of Radon Emanation Measurements for Mineral, Rock, Soil, Mill Tailing and Fly Ash.” *Applied Radiation and Isotopes* 69 (10): 1422–35. https://doi.org/10.1016/j.apradiso.2011.06.009.

Sramek, Ondrej, Lauren Stevens, William F. McDonough, Sujoy Mukhopadhyay, and R. J. Peterson. 2017. “Subterranean Production of Neutrons, 39Ar and 21Ne: Rates and Uncertainties.” *Geochimica et Cosmochimica Acta* 196: 370–87. https://doi.org/10.1016/j.gca.2016.09.040.

Williams, R. M., C. E. Aalseth, J. M. Brandenberger, A. R. Day, E. Finn, E. S. Fuller, E. W. Hoppe, et al. 2017. “Development of a Low-Level 39Ar Calibration Standard – Analysis by Absolute Gas Counting Measurements Augmented with Simulation.” *Applied Radiation and Isotopes* 126 (February): 243–48. https://doi.org/10.1016/j.apradiso.2017.02.018.

Wilson, William H. W.H., Christine M. C.M. Johnson, Justin D. J.D. Lowrey, Steven R. S.R. Biegalski, and D.A. Derek A. Haas. 2015. “Cosmic-Ray Induced Production of Radioactive Noble Gases in the Atmosphere, Ground, and Seawater.” *Journal of Radioanalytical and Nuclear Chemistry* 305 (1): 183–92. https://doi.org/10.1007/s10967-015-4181-7.

PNNL-30868

Pacific Northwest National Laboratory

902 Battelle Boulevard
P.O. Box 999
Richland, WA 99354
1-888-375-PNNL (7665)

www.pnnl.gov